Available online at www.sciencedirect.com
ScienceDirect
International Journal of Solids and Structures 44 (2007) 834–859
INTERNATIONAL JOURNAL OF SOLIDS and STRUCTURES
www.elsevier.com/locate/ijsolstr

The Mechanical Threshold Stress model for various tempers of AISI 4340 steel

Biswajit Banerjee *

Department of Mechanical Engineering, University of Utah, Salt Lake City, UT 84112, USA

Received 2 September 2005; received in revised form 31 March 2006
Available online 17 May 2006

Abstract

Numerical simulations of high strain rate and high temperature deformation of pure metals and alloys require realistic plastic constitutive models. Empirical models include the widely used Johnson–Cook model and the semi-empirical Steinberg–Cochran–Guinan–Lund model. Physically based models such as the Zerilli–Armstrong model, the Mechanical Threshold Stress model, and the Preston–Tonks–Wallace model are also coming into wide use. In this paper, we determine the Mechanical Threshold Stress model parameters for various tempers of AISI 4340 steel using experimental data from the open literature. We also compare stress–strain curves and Taylor impact test profiles predicted by the Mechanical Threshold Stress model with those from the Johnson–Cook model for 4340 steel. Relevant temperature- and pressure-dependent shear modulus models, melting temperature models, a specific heat model, and an equation of state for 4340 steel are discussed and their parameters are presented.

Keywords: Constitutive behavior; Plasticity; High strain rate; High temperature; Finite strain; Elastic–viscoplastic material; Impact testing

1. Introduction

The present work was motivated by the need to simulate numerically the deformation and fragmentation of a heated AISI 4340 steel cylinder loaded by explosive deflagration. Such simulations require a plastic constitutive model that is valid over temperatures ranging from 250 K to 1300 K and over strain rates ranging from quasi-static to the order of $10^5\ s^{-1}$. The Mechanical Threshold Stress (MTS) model (Follansbee and Kocks, 1988; Kocks, 2001) is a physically based model that can be used for the range of temperatures and strain rates of interest in these simulations. In the absence of any MTS models specifically for 4340 steels, an existing MTS model for HY-100 steel (Goto et al., 2000a,b) was initially explored as a surrogate for 4340 steel. However, the HY-100 model failed to produce results that were in agreement with experimental stress–strain data for 4340 steel. This paper attempts to redress that issue by providing the MTS parameters for a number of tempers of 4340 steel (classified by their Rockwell C hardness number). The MTS model is compared with the Johnson–Cook (JC)

* Tel.: +1 801 585 5239; fax: +1 801 585 0039.
E-mail address: banerjee@eng.utah.edu

0020-7683/$ - see front matter © 2006 Elsevier Ltd. All rights reserved.
doi:10.1016/j.ijsolstr.2006.05.022

model (Johnson and Cook, 1983, 1985) for 4340 steel and the relative advantages and disadvantages of these models are discussed.

The MTS model requires a temperature and pressure dependent elastic shear modulus. Three such shear modulus models and the associated melting temperature models are discussed in this paper. Conversion of plastic work into heat is achieved through a specific heat model that takes the transformation from the bcc (α) phase to the fcc (γ) phase into account. The associated Mie–Grüneisen equation of state for the pressure is also discussed.

The organization of this paper is as follows. The MTS model is described in Section 2. The procedure used to determine the parameters of the MTS model parameters are given in Section 3. Predictions from the MTS model are compared with those from the Johnson–Cook model in Section 4. These comparisons include both stress–strain curves and Taylor impact tests. Conclusions and final remarks are presented in Section 6. Details of the determination of parameters for the models required by the MTS model (for example, the shear modulus model) and their validation are given in Appendix A.

Notation: The following notation has been used in the equations that follow. Other symbols that appear in the text are identified following the relevant equations.

$\dot{\epsilon}$	strain rate
ϵ_p	plastic strain
μ	shear modulus
ρ	current mass density
ρ_0	initial mass density
$\eta = \rho/\rho_0$	compression
σ_y	yield stress
b	magnitude of the Burgers vector
k_b	Boltzmann constant
p	pressure (positive in compression)
C_p	specific heat at constant pressure
C_v	specific heat at constant volume
T	temperature
T_m	melting temperature

2. Mechanical Threshold Stress model

The Mechanical Threshold Stress (MTS) model (Follansbee and Kocks, 1988; Goto et al., 2000b) gives the following form for the flow stress

$$\sigma_y(\epsilon_p, \dot{\epsilon}, T) = \sigma_a + (S_i\sigma_i + S_e\sigma_e)\frac{\mu(p,T)}{\mu_0} \tag{1}$$

where σ_a is the athermal component of mechanical threshold stress, σ_i is the intrinsic component of the flow stress due to barriers to thermally activated dislocation motion, σ_e is the strain hardening component of the flow stress, (S_i, S_e) are strain-rate and temperature dependent scaling factors, and μ_0 is the shear modulus at 0 K and ambient pressure.

The athermal component of the yield stress is a function of grain size, dislocation density, distribution of solute atoms, and other long range barriers to dislocation motion. A simple model for this component can be written as (Zerilli and Armstrong, 1987; Nemat-Nasser, 2004):

$$\sigma_a = \left(\sigma_0 + C_1\epsilon_p^n + \frac{k}{\sqrt{d}}\right)\frac{\mu(p,T)}{\mu_0} \tag{2}$$

where σ_0 is the component due to far field dislocations. The second term represents the dependence on dislocation density and C_1, n are constants. The third term represents the Hall–Petch effect where k is a material constant and d is the grain size.

The scaling factors S_i and S_e have the modified Arrhenius form

$$S_i = \left[1 - \left(\frac{k_b T}{g_{0i} b^3 \mu(p,T)} \ln \frac{\dot{\epsilon}_{0i}}{\dot{\epsilon}}\right)^{1/q_i}\right]^{1/p_i} \quad (3)$$

$$S_e = \left[1 - \left(\frac{k_b T}{g_{0e} b^3 \mu(p,T)} \ln \frac{\dot{\epsilon}_{0e}}{\dot{\epsilon}}\right)^{1/q_e}\right]^{1/p_e} \quad (4)$$

where (g_{0i}, g_{0e}) are normalized activation energies, $(\dot{\epsilon}_{0i}, \dot{\epsilon}_{0e})$ are constant reference strain rates, and (q_i, p_i, q_e, p_e) are constants. The strain hardening component of the mechanical threshold stress (σ_e) is given by a modified Voce law

$$\frac{d\sigma_e}{d\epsilon_p} = \theta(\sigma_e) \quad (5)$$

where

$$\theta(\sigma_e) = \theta_0[1 - F(\sigma_e)] + \theta_1 F(\sigma_e) \quad (6)$$

$$\theta_0 = a_{00} + a_{10} \ln \dot{\epsilon} + a_{20} \sqrt{\dot{\epsilon}} + a_{30} T \quad (7)$$

$$\theta_1 = a_{01} + a_{11} \ln \dot{\epsilon} + a_{21} \sqrt{\dot{\epsilon}} + a_{31} T \quad (8)$$

$$F(\sigma_e) = \frac{\tanh\left(\alpha \frac{\sigma_e}{\sigma_{es}}\right)}{\tanh(\alpha)} \quad (9)$$

$$\ln\left(\frac{\sigma_{es}}{\sigma_{0es}}\right) = \left(\frac{k_b T}{g_{0es} b^3 \mu(p,T)}\right) \ln\left(\frac{\dot{\epsilon}}{\dot{\epsilon}_{0es}}\right) \quad (10)$$

and θ_0 is the strain hardening rate due to dislocation accumulation, θ_1 is a saturation hardening rate (usually zero), $(a_{0j}, a_{1j}, a_{2j}, a_{3j}, \alpha)$ are constants ($j = 0, 1$), σ_{es} is the saturation stress at zero strain hardening rate, σ_{0es} is the saturation threshold stress for deformation at 0 K, g_{0es} is the associated normalized activation energy, and $\dot{\epsilon}_{0es}$ is the reference maximum strain rate. Note that the maximum strain rate for which the model is valid is usually limited to approximately $10^7\ s^{-1}$.

3. Determination of MTS model parameters

The yield strength of high-strength low-alloy (HSLA) steels such as 4340 steel can vary dramatically depending on the heat treatment that it has undergone. This is due to the presence of bcc ferrite-bainite phases along with the dominant bcc martensite phase at room temperature. At higher temperatures (below the α–γ transition) the phases partially transform into the fcc austenite and much of the effect of heat treatment is expected to be lost. Beyond the transition temperature, the alloy is mostly the fcc γ phase that is expected to behave differently than the lower temperature phases. Hence, empirical plasticity models of 4340 steel have to be recalibrated for different levels of hardness and for different ranges of temperature.

In the absence of relevant microstructural models for the various tempers of 4340 steel, we assume that there is a direct correlation between the Rockwell C hardness of the alloy steel and the yield stress (see the ASM Handbook, Steiner, 1990). In this section, we determine the MTS parameters for four tempers of 4340 steel. Empirical relationships are then derived that can be used to calculate the parameters of intermediate tempers of 4340 steel via interpolation.

The tempers of 4340 steel that we have used to determine the MTS model parameters are shown in Table 1. All the data are for materials that have been oil quenched after austenitization. The 4340 VAR (vacuum arc remelted) steel has a higher fracture toughness than the standard 4340 steel. However, both steels have similar yield behavior (Brown et al., 1996).

The experimental data are either in the form of true stress versus true strain or shear stress versus average shear strain. These curves were digitized manually with care and corrected for distortion. The error in digitization was around 1% on average. The shear stress–strain curves were converted into an effective tensile

Table 1
Sources of experimental data for 4340 steel

Material	Hardness	Normalize temp. (°C)	Austenitize temp. (°C)	Tempering temp. (°C)	Reference
4340 Steel	R_c 30				Johnson and Cook (1985)
4340 Steel	R_c 38	900	870	557	Larson and Nunes (1961)
4340 Steel	R_c 38		850	550	Lee and Yeh (1997)
4340 VAR Steel	R_c 45	900	845	425	Chi et al. (1989)
4340 VAR Steel	R_c 49	900	845	350	Chi et al. (1989)

stress–strain curves assuming von Mises plasticity (see Goto et al., 2000a). The elastic portion of the strain was then subtracted from the total strain to get true stress versus plastic strain curves. The elastic part of the strain was computed using a Poisson's ratio of 0.29 and the temperature dependent shear modulus from the Nadal–Le Poac (NP) model (see Appendix A).

3.1. Determination of σ_a

The first step in the determination of the parameters for the MTS models is the estimation of the athermal component of the yield stress (σ_a). This parameter is dependent on the Hall–Petch effect and hence on the characteristic martensitic packet size. The packet size will vary for various tempers of steel and will depend on the size of the austenite crystals after the α–γ phase transition. Since we do not have unambiguous grain sizes and other information needed to determine σ_a, we assume that σ_a is constant and independent of temper. We have used a value of 50 MPa based on the value used for HY-100 steel (Goto et al., 2000a).

From Eqs. (2) and (1) we can see that if we consider σ_a to be constant, then part of the athermal effects will be manifested in the intrinsic part of the mechanical threshold stress (σ_i). This is indeed what we observe during the determination of σ_i in the next section.

3.2. Determination of σ_i and g_{0i}

From Eq. (1), it can be seen that σ_i can be found if σ_y and σ_a are known and σ_e is zero. Assuming that σ_e is zero when the plastic strain is zero, and using Eq. (3), we get the relation

$$\left(\frac{\sigma_y - \sigma_a}{\mu}\right)^{p_i} = \left(\frac{\sigma_i}{\mu_0}\right)^{p_i}\left[1 - \left(\frac{1}{g_{0i}}\right)^{1/q_i}\left[\frac{k_b T}{\mu b^3}\ln\left(\frac{\dot{\epsilon}_{0i}}{\dot{\epsilon}}\right)\right]^{1/q_i}\right] \tag{11}$$

Modified Arrhenius (Fisher) plots based on Eq. (11) are used to determine the normalized activation energy (g_{0i}) and the intrinsic thermally activated portion of the yield stress (σ_i). The parameters p_i and q_i for iron and steels (based on the effect of carbon solute atoms on thermally activated dislocation motion) have been suggested to be 0.5 and 1.5, respectively (Kocks et al., 1975; Goto et al., 2000a). Alternative values can be obtained depending on the assumed shape of the activation energy profile or the obstacle force–distance profile (Cottrell and Bilby, 1949; Caillard and Martin, 2003).

We have observed that the values suggested for HY-100 give us a value of the normalized activation energy g_{0i} for $R_c = 30$ that is around 40, which is not physical. Instead, we have assumed a rectangular force–distance profile which gives us values of $p_i = 2/3$ and $q_i = 1$ and reasonable values of g_{0i}. We have assumed that the reference strain rate is $\dot{\epsilon}_{0i} = 10^8\ \mathrm{s}^{-1}$.

The Fisher plots of the raw data (based on Eq. (11)) are shown as squares in Fig. 1(a)–(d). Straight line least squares fits to the data are also shown in the figures. For these plots, the shear modulus (μ) has been calculated using the NP shear modulus model discussed in Appendix A.3. The yield stress at zero plastic strain (σ_y) is the intersection of the stress–plastic strain curve with the stress axis. The value of the Boltzmann constant (k_b) is 1.3806503e−23 J/K and the magnitude of the Burgers vector (b) is assumed to be 2.48e−10 m. The density of the material is assumed to be constant with a value of 7830 kg/m^3. The raw data used in these plots can be found elsewhere (Banerjee, 2005).

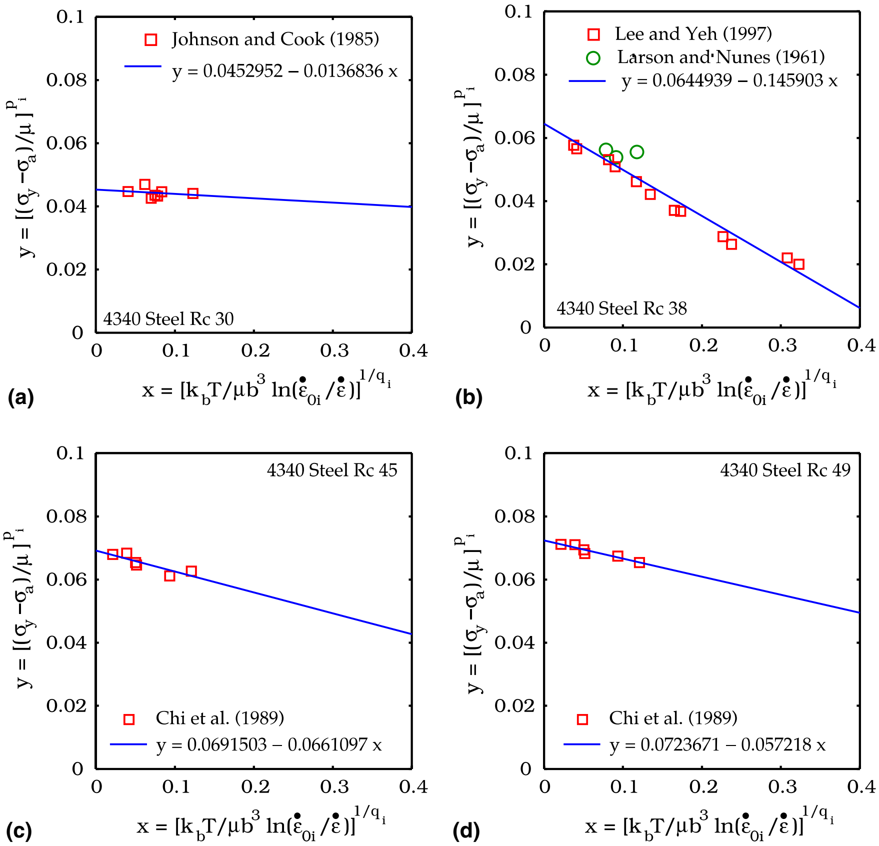

Fig. 1. Fisher plots for the intrinsic component of the MTS model for various tempers of 4340 steel. Experimental data are from Larson and Nunes (1961), Johnson and Cook (1985), Chi et al. (1989), and Lee and Yeh (1997). $\sigma_a = 50$ MPa, $p_i = 2/3$, $q_i = 1$, $\dot{\epsilon}_{0i} = 10^8\ s^{-1}$, $k_b = 1.3806503e{-}23$ J/K, $b = 2.48e{-}10$ m. (a) $R_c = 30$, (b) $R_c = 38$, (c) $R_c = 45$ and (d) $R_c = 49$.

The spread in the data for R_c 30 (Fig. 1(a)) is quite large and a very low R^2 value is obtained for the fit. This is partially due to the inclusion of both tension and shear test data (in the form of effective tensile stress) in the plot. Note that significantly different yield stresses can be obtained from tension and shear tests (especially at large strains) (Johnson and Cook, 1985; Goto et al., 2000a). However, this difference is small at low strains and is not expected to affect the intrinsic part of the yield stress much. A more probable cause of the spread is that the range of temperatures and strain rates is quite limited. More data at higher strain rates and temperatures are needed to get an improved correlation for the R_c 30 temper of 4340 steel.

Fig. 1(b) shows the fit to the Fisher plot data for 4340 steel of hardness R_c 38. The low strain rate data from Larson and Nunes (1961) are the outliers near the top of the plot. The hardness of this steel was estimated from tables given in the ASM Handbook (Steiner, 1990) based on the heat treatment but could possibly be higher than R_c 38. However, the Larson and Nunes (1961) data are close to the data from Lee and Yeh (1997) as can be seen from the plot. A close examination of the high temperature data shows that there is a small effect due to the α to γ phase transformation at high temperatures.

The stress–strain data for 4340 steel R_c 45 shows an anomalous temperature dependent behavior under quasistatic conditions in that the yield stress at 373 K is higher than that at 298 K. The fit to the Fisher plot data for this temper of steel is shown in Fig. 1(c). The fit to the data can be improved if the value of σ_a is assumed to be 150 MPa and q_i is assumed to be equal to 2. However, larger values of σ_a can lead to large negative values of σ_e at small strains – which is unphysical.

The fit to the Fisher data for the R_c 49 temper is shown in Fig. 1(d) and is reasonably good. More data at high strain rates and high temperatures are needed for both the R_c 45 and the R_c 49 tempers of 4340 steel for improved estimates of the intrinsic part of the yield stress.

The values of σ_i and g_{0i} for the four tempers of 4340 are shown in Table 2. The value of g_{0i} for the R_c 38 temper is quite low and leads to values of the Arrhenius factor (S_i) that are zero for temperatures greater than 800 K. In the following section, we consider the effect of dividing the R_c 38 data into high and low temperature regions to alleviate this problem.

3.2.1. High temperature values of σ_i and g_{0i}

More data at higher temperatures and high strain rates are required for better characterization of the R_c 30, R_c 45, and R_c 49 tempers of 4340 steel. In the absence of high temperature data, we can use data for the R_c 38 temper at high temperatures to obtain the estimates of σ_i and g_{0i} for other tempers.

The temperature at which the α to γ phase transition occurs is 1040 K. We divide the temperature regime into two parts: $T_0 < 1040$ K and $T_0 \geqslant 1040$ K. We assume that the various tempers retain distinctive properties up to the phase transition temperature. All the tempers are assumed to have identical values of σ_i and g_{0i} above 1040 K. A detailed exploration of various temperature regimes can be found in Banerjee (2005).

The two-regime fits to the Fisher plot data for R_c 38 are shown in Fig. 2. The values of σ_i and g_{0i} for the R_c 38 temper (in the α phase) are 1528 MPa and 0.412, respectively, while those for the γ phase are 896 MPa and 0.576, respectively. The fits show a jump in value at 1040 K that is not ideal for Newton iterations in a typical elastic–plastic numerical code. We suggest that the γ phase values of these parameters be used if there is any problem with convergence.

Plots of σ_i and g_{0i} as functions of the Rockwell hardness number (for temperatures below 1040 K) are shown in Fig. 3(a) and (b), respectively. Straight line fits to the σ_i and g_{0i} versus R_c data can be used to estimate these parameters for intermediate tempers of the α phase of 4340 steel. These fits are also shown in Fig. 3(a) and (b).

The higher hardness tempers of 4340 steel are obtained by quenching at lower temperatures. As the hardness increases, the grain size becomes smaller due the faster rate of quenching. Recall that we have assumed that the value of the athermal component of the yield stress (σ_a) is constant. A portion of the temper dependent athermal effects (such as the Hall–Petch effect) manifest themselves in the intrinsic part (σ_i) of the mechanical threshold stress at 0 K. Therefore we observe an increase in the value of σ_i with increasing hardness of temper.

Table 2
Values of σ_i and g_{0i} for four tempers of 4340 steel

Hardness (R_c)	σ_i (MPa)	g_{0i}
30	867.6	3.31
38	1474.1	0.44
45	1636.6	1.05
49	1752	1.26

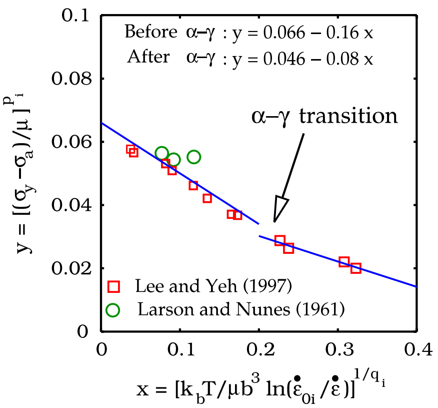

Fig. 2. Fisher plots for the intrinsic component of the MTS model for the α and γ phases of R_c 38 4340 steel assuming two temperature regimes.

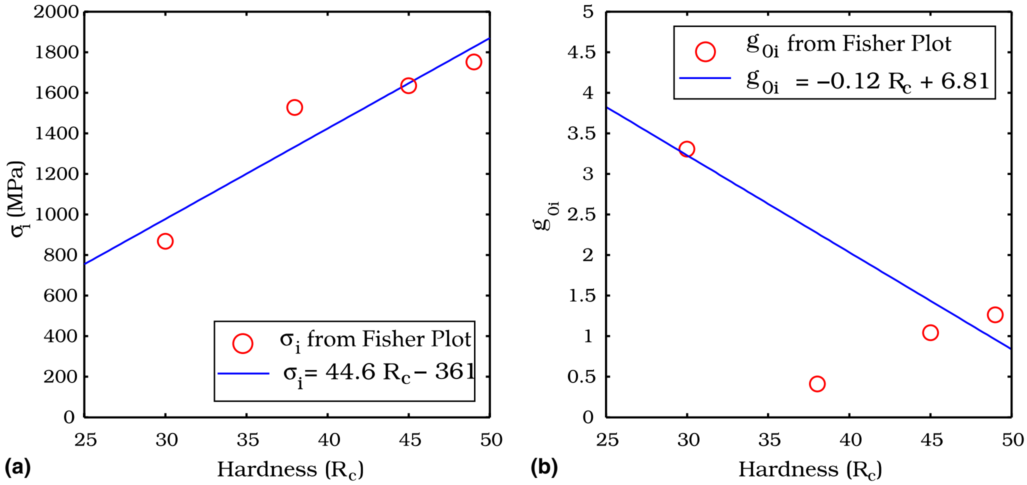

Fig. 3. Values of σ_i and g_{0i} obtained from the Fisher plots for various tempers of the α phase of 4340 steel. The fit for g_{0i} excludes the low value for R_c 38 4340 steel. (a) $\sigma_i = 44.628R_c - 361.33$ MPa (b) $g_{0i} = -0.1195R_c + 6.814$.

We would expect the normalized activation energy g_{0i} to vary little between the various tempers. It is not clear whether the trend that we observe in Fig. 3(b) is physical. The value of g_{0i} for the R_c 38 temper appears to be unusually low. However, these values lead to good fit to experimental data for R_c 38 temper. For that reason, we have used these values of σ_i and g_{0i} for all subsequent computations that use these parameters.

3.3. Determination of σ_{0es} and g_{0es}

Once estimates have been obtained for σ_i and g_{0i}, the value of $S_i\sigma_i$ can be calculated for a particular strain rate and temperature. From Eq. (1), we then get

$$\sigma_e = \frac{1}{S_e}\left[\frac{\mu_0}{\mu}(\sigma_y - \sigma_a) - S_i\sigma_i\right]. \tag{12}$$

Eq. (12) can be used to determine the saturation value (σ_{es}) of the structural evolution stress (σ_e). Given a value of σ_{es}, Eq. (10) can be used to compute σ_{0es} and the corresponding normalized activation energy (g_{0es}) from the relation

$$\ln(\sigma_{es}) = \ln(\sigma_{0es}) - \frac{k_b T}{g_{0es} b^3 \mu} \ln\left(\frac{\dot{\epsilon}}{\dot{\epsilon}_{0es}}\right). \tag{13}$$

Following Goto et al. (2000a), we assume that $\dot{\epsilon}_{0e}$, $\dot{\epsilon}_{0es}$, p_e, q_e, and g_{0e} take the values $10^7\ \mathrm{s}^{-1}$, $10^7\ \mathrm{s}^{-1}$, 2/3, 1, and 1.6, respectively. These values are used to calculate S_e at various temperatures and strain rates. The values of σ_i and g_{0i} vary with hardness for temperatures below 1040 K, and are constant above that temperature as discussed in the previous section. Adiabatic heating is assumed for strain rates greater than $500\ \mathrm{s}^{-1}$.

The value of σ_{es} can be determined either from a plot of σ_e versus the plastic strain or from a plot of the tangent modulus $\theta(\sigma_e)$ versus σ_e. Representative plots of σ_e versus the plastic strain are shown in Fig. 4(a) and the corresponding θ versus σ_e plots are shown in Fig. 4(b). The plotted value of the tangent modulus (θ) is the mean of the tangent moduli at each value of σ_e (except for the end points where a single value is used). The saturation stress (σ_{es}) is the value at which σ_e becomes constant or θ is zero. Note that errors in the fitting of σ_i and g_{0i} can cause the computed value of σ_e to be nonzero at zero plastic strain.

Fig. 5(a)–(d) show the Fisher plots used to compute σ_{0es} and g_{0es} for the four tempers of 4340 steel. The raw data for these plots can be found in Banerjee (2005).

The correlation between the modified Arrhenius relation and the data is quite poor. Considering the fact that special care has been taken to determine the value of σ_{es}, the poor fit appears to suggest that the strain

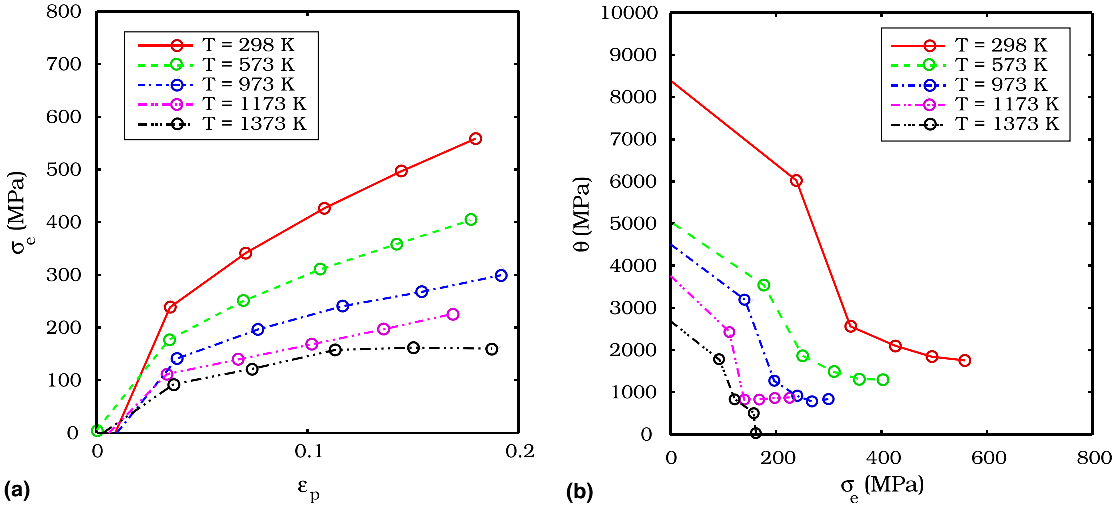

Fig. 4. An example of the curves used to determine the saturation value (σ_{es}) of the structure evolution stress (σ_e). The saturation stress is the value at which the rate of hardening (θ) zero. The experimental data are from Lee and Yeh (1997) for a strain rate of 1500 s^{-1} and the R_c 38 temper. (a) σ_e versus ϵ_p (R_c 38 1500 s^{-1}) and (b) θ versus σ_e (R_c 38 1500 s^{-1}).

dependent part of the mechanical threshold stress does not follow an Arrhenius relation. However, we do not know the error bounds of the experimental data and therefore cannot be confident about such a conclusion.

Values of σ_{0es} and g_{0es} computed from the Fisher plots are shown in Table 3. Straight line fits to the data are shown in Fig. 6(a) and (b). The value of the saturation stress decreases with increasing hardness while the normalized activation energy (at 0 K) increases with increasing hardness.

These trends suggest that as the grain size decreases, the flow stress saturates earlier relative to the initial yield stress. In addition, for harder tempers, larger amounts of energy are required to further harden the material beyond the initial yield stress. This effect is probably because the energy needed to transport dislocations across grain boundaries decreases as the hardness of the temper increases and the grain size decreases. The grain boundary barriers are easier to overcome and the material appears to flow without hardening.

In the numerical simulations that follow, we have used a median value of 0.284 for g_{0es} and the mean value of 705.5 MPa for σ_{0es} for intermediate tempers of 4340 steel. Fits to the data for temperatures greater than 1040 K give us values of σ_{0es} and g_{0es} for the γ phase of 4340 steel. The values of these parameters at such high temperatures are $g_{0es} =$ 0.294 and $\sigma_{0es} = 478.36$ MPa.

3.4. Determination of hardening rate (θ)

The modified Voce rule for the hardening rate (θ) (Eq. (6)) is purely empirical. To determine the temperature and strain rate dependence of θ, we plot the variation of θ versus the normalized structure evolution stress assuming a hyperbolic tangent dependence of the rate of hardening on the mechanical threshold stress. We assume that $\alpha = 3$.

Fig. 7(a)–(d) show some representative plots of the variation of θ with $F := \tanh(\alpha\sigma_e/\sigma_{es})/\tanh(\alpha)$. As the plots show, the value of θ_1 (the value of θ at $F = 1$) can be assumed to be zero for most of the data.

It is observed from Fig. 7(a) that there is a strong strain rate dependence of θ that appears to override the expected decrease with increase in temperature for the R_c 30 temper of 4340 steel. It can also been seen that θ is almost constant at 298 K and 0.002 s^{-1} strain rate which implies linear hardening. However, the hyperbolic tangent rule appears to be a good approximation at higher temperatures and strain rates.

The plot for the R_c 38 temper of 4340 steel (Fig. 7(b)) shows a strong temperature dependence of θ; the hardening rate decreases with increasing temperature. The same behavior is observed for all high strain rate data. However, for the low strain rate of 0.0002 s^{-1}, there is an increase in θ with increasing temperature.

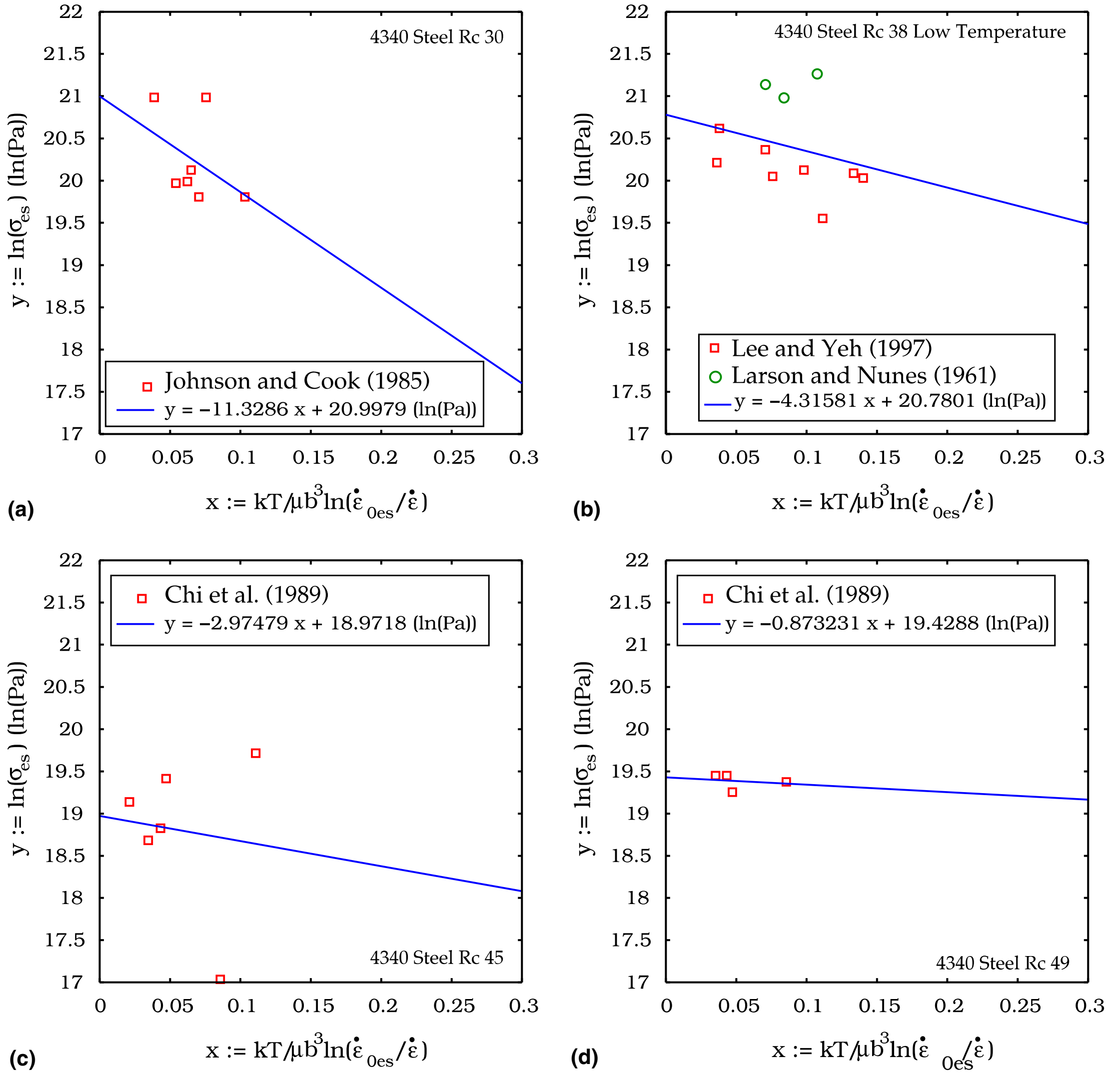

Fig. 5. Fisher plots for the structure evolution dependent component of the MTS model for the α phase of various tempers of 4340 steel. Experimental data are from Larson and Nunes (1961), Johnson and Cook (1985), Chi et al. (1989), and Lee and Yeh (1997). $\dot{\epsilon}_{0e} = 10^7$, $\dot{\epsilon}_{0es} = 10^7$, $p_e = 2/3$, $q_e = 1$, and $g_{0e} = 1.6$. (a) $R_c = 30$, (b) $R_c = 38$, (c) $R_c = 45$ and (d) $R_c = 49$.

Table 3
Values of σ_{0es} and g_{0es} for four tempers of 4340 steel

Hardness (R_c)	σ_{0es} (MPa)	g_{0es}
30	1316.1	0.088
38	1058.4	0.232
45	173.5	0.336
49	274.9	1.245

Fig. 7(c) and (d) also show an increase in θ with temperature. These reflect an anomaly in the plastic behavior of 4340 steel for relatively low temperatures (below 400 K) (Tanimura and Duffy, 1986) that cannot be modeled using a linear Arrhenius law.

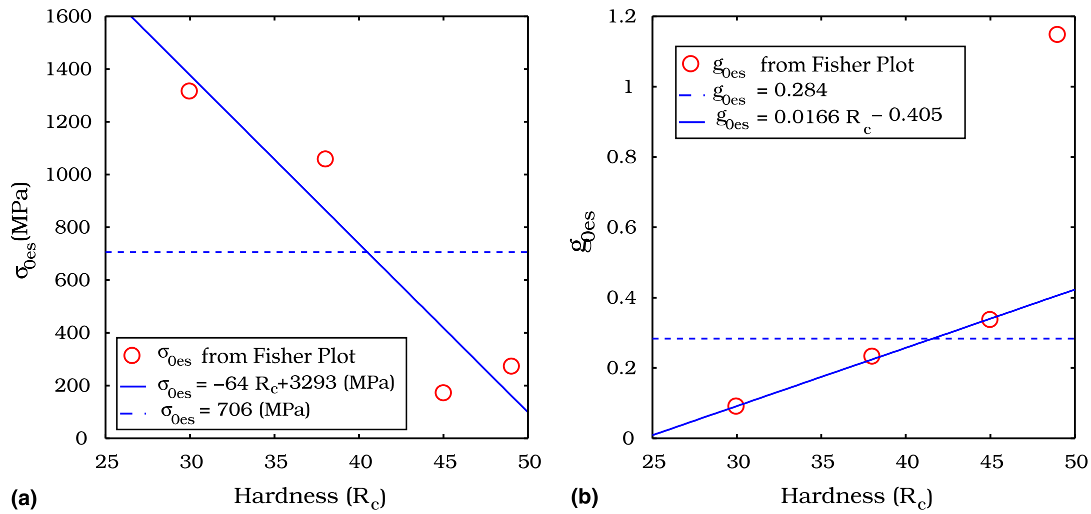

Fig. 6. Values of σ_{0es} and g_{0es} obtained from the Fisher plots for various tempers of the α phase of 4340 steel. The dashed lines show the median values of the parameters. (a) $\sigma_{0es} = -63.9R_c + 3293.4$ (MPa) and (b) $g_{0es} = 0.01656R_c - 0.405$.

More fits to the experimental data of the form shown in Eq. (7) can be found in Banerjee (2005). In general, the strain rate dependence of the hardening rate is small compared to the temperature dependence. Also, the different tempers cannot be distinguished for each other as far as the hardening rate is concerned. Therefore, we ignore the strain rate dependence of the hardening rate and fit a curve to all the data taking only temperature dependence into account (as shown in Fig. 8). Distinctions have not been made between various tempers of 4340 steel in the plot. However, the data are divided into two regimes based on the α–γ phase transition temperature.

The resulting equations for θ_0 as functions of temperature are

$$\theta_0 = \begin{cases} 15719 - 10.495T(\text{MPa}) & \text{for } T < 1040\,K \\ 7516 - 3.7796T(\text{MPa}) & \text{for } T > 1040\,K \end{cases} \tag{14}$$

This completes the determination of the parameters for the MTS model.

4. Comparison of MTS model predictions and experimental data

The performance of the MTS model for 4340 steel is compared to experimental data in this section. In the figures that follow, the MTS predictions are shown as dotted lines while the experimental data are shown as solid lines with symbols indicting the conditions of the test. Isothermal conditions have been assumed for strain rates less than 500 s^{-1} and adiabatic heating is assumed to occurs at higher strain rates.

Fig. 9(a) and (b) show the experimental stress–strain curves and the corresponding MTS predictions for the R_c 30 temper of 4340 steel. The model matches the experimental curves quite well for low strain rates (keeping in mind the difference between the stress–strain curves in tension and in shear). The high strain rate curves are also accurately reproduced though there is some error in the initial hardening modulus for the 650 s^{-1} and 735 K case. This error can be eliminated if the effect of strain rate is included in the expression for θ_0. The maximum modeling error for this temper varies between 5% and 10%.

Recall that we did not use R_c 32 experimental data to fit the MTS model parameters. As a check of the appropriateness of the relation between the parameters and the R_c hardness number, we have plotted the MTS predictions versus the experimental data for this temper in Fig. 10. Our model predicts a stronger temperature dependence for this temper than the experimental data. However, the initial high temperature yield stress is reproduced quite accurately while the ultimate tensile stress is reproduced well for the lower temperatures.

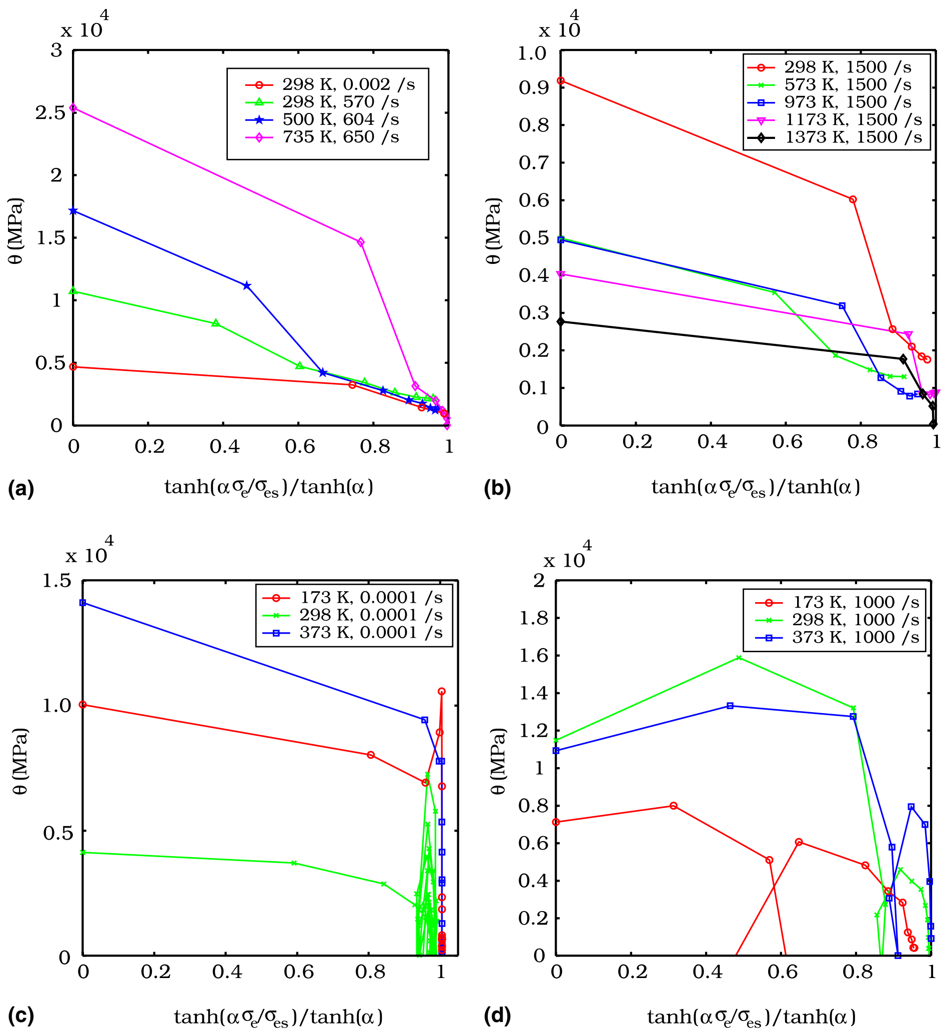

Fig. 7. Shear representative examples of curves used to determine the initial hardening rate θ_0 of various tempers of 4340 steel as a function of temperature and strain rate. The experimental data are from the following sources: R_c 30 (Johnson and Cook, 1985), R_c 38 (Lee and Yeh, 1997), R_c 45 and 49 (Chi et al., 1989) $\alpha = 3$. (a) R_c 30, tension; (b) R_c 38, compression; (c) R_c 45, shear and (d) R_c 49, shear.

The low strain rate stress–strain curves for R_c 38 4340 steel are shown in Fig. 11(a). High strain rate stress–strain curves for the R_c 38 temper are shown in Fig. 11(b)–(d). The saturation stress predicted at low strain rates is around 20% smaller than the observed values at large strains. The high strain rate data are reproduced quite accurately by the MTS model with a modeling error of around 5% for all temperatures.

Experimental data for the R_c 45 temper are compared with MTS predictions in Fig. 12(a) and (b). The MTS model underpredicts the low strain rate yield stress and initial hardening modulus by around 15% for both the 173 K and 373 K data. The prediction is within 10% for the 298 K data. The anomaly at 373 K is clearly visible for the low strain rate plots shown in Fig. 12(a). The high strain rate data are reproduced quite accurately for all three temperatures and the error is less than 10%.

Comparisons for the R_c 49 temper are shown in Fig. 13(a) and (b). The model predicts the experimental data quite accurately for 173 K and 298 K at a strain rate of 0.0001 s^{-1}. As expected, the anomalous behavior at 373 K is not predicted and a modeling error of around 15% is observed for this temperature. For the high strain rate cases shown in Fig. 13(b), the initial hardening modulus is under-predicted and saturation is predicted at a lower stress than observed. In this case, the modeling error is around 10%.

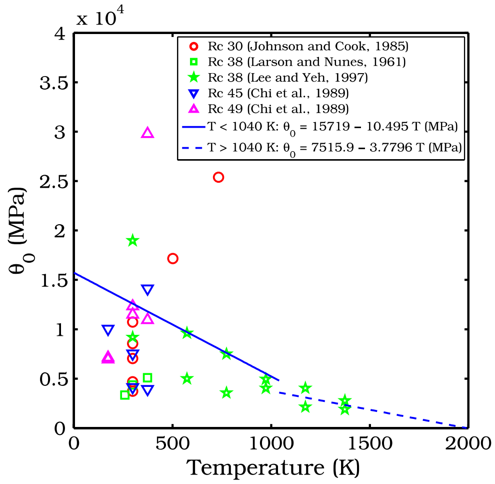

Fig. 8. Variation of θ_0 with temperature. Experimental data are shown as symbols and the linear fits to the data are shown as straight lines.

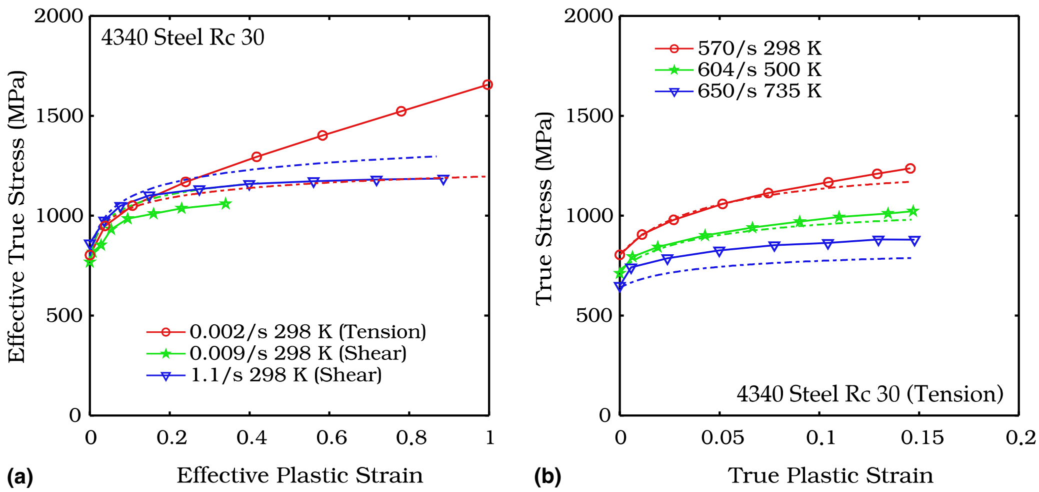

Fig. 9. Comparison of MTS prediction with experimental data from Johnson and Cook, 1985 for the R_c 30 temper of 4340 steel. The MTS predictions are shown as dashed lines. (a) Low strain rates (tension and shear tests) and (b) high strain rates (tension tests).

The comparisons of the MTS model predictions with experimental data shows that the predictions are all within an error of 20% for the range of data examined. If we assume that the standard deviation of the experimental data is around 5% (Hanson, 2005) then the maximum modeling error is around 15% with a 5% mean error. This error is quite acceptable for numerical simulations, provided the simulations are conducted within the range of conditions used to fit the data.

5. MTS model predictions over an extended range of conditions

In this section, we compare the yield stresses predicted for a R_c 40 temper of 4340 steel by the MTS model with those predicted by the Johnson–Cook (JC) model. A large range of strain rates and temperatures is explored. In the plots shown below, the yield stress (σ_y) is the Cauchy stress, the plastic strain (ϵ_p) is the true plastic strain, the temperatures (T) are the initial temperatures and the strain rates $\dot{\epsilon}$ are the nominal strain rates. The effect of pressure on the density and melting temperature has been ignored in the MTS calculations presented in this section. The Johnson–Cook model and relevant parameters are discussed in Appendix B.

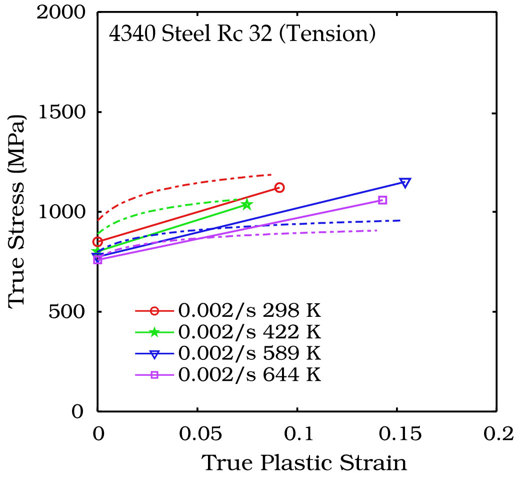

Fig. 10. Comparison of MTS prediction with experimental data from Brown et al. (1996) for the R_c 32 temper of 4340 steel. The data are from tension tests. The dashed lines show the MTS predictions.

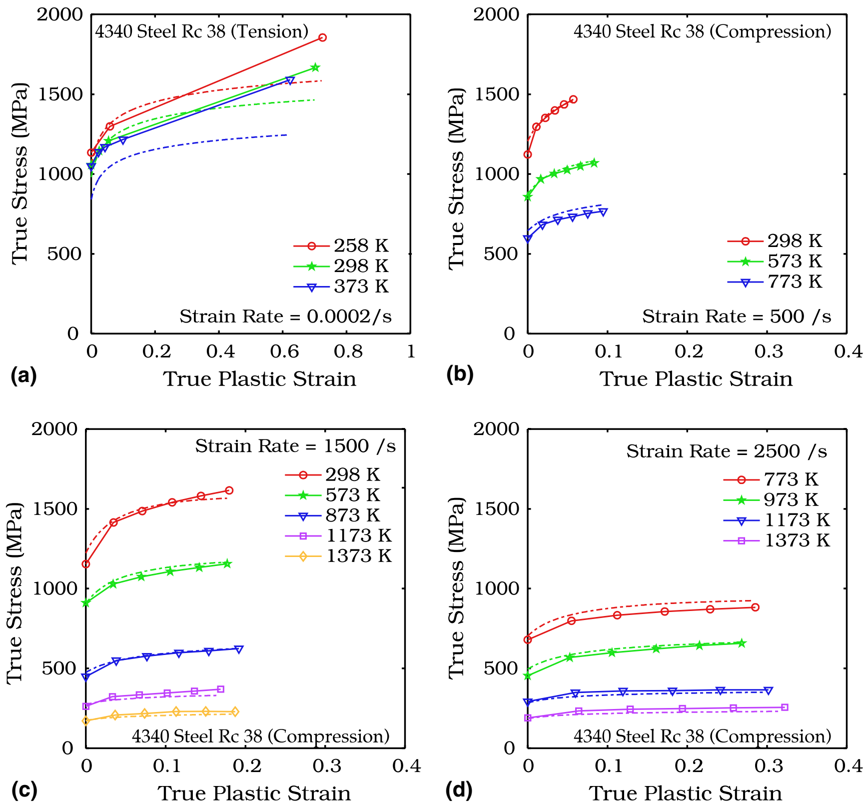

Fig. 11. Comparison of MTS prediction with experimental data from Larson and Nunes (1961) and Lee and Yeh (1997) for the R_c 38 temper of 4340 steel at various strain rates. The dashed lines show the MTS predictions. (a) Tension tests at 0.0002 s^{-1} (Larson and Nunes, 1961). (b) Compression tests at 500 s^{-1} (Lee and Yeh, 1997). (c) Compression tests at 1500 s^{-1} (Lee and Yeh, 1997). (d) Compression tests at 2500 s^{-1} (Lee and Yeh, 1997).

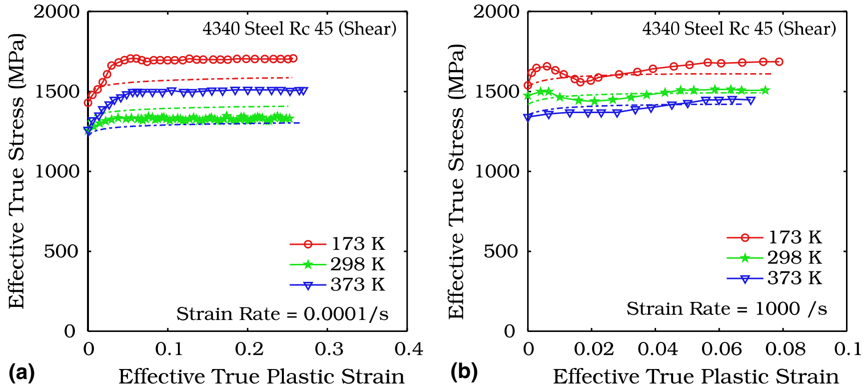

Fig. 12. Comparison of MTS prediction with experimental data from Chi et al. (1989) for the R_c 45 temper of 4340 steel. The dashed lines show the MTS predictions. Shear tests at (a) 0.0001 s^{-1} and (b) 1000 s^{-1}.

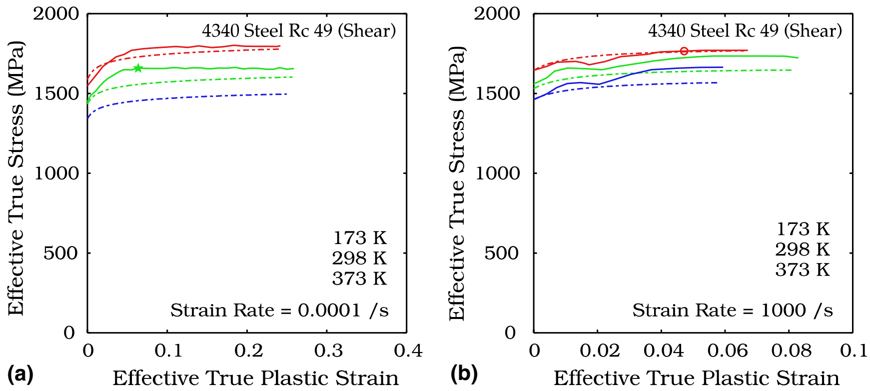

Fig. 13. Comparison of MTS prediction with experimental data from Chi et al. (1989) for the R_c 49 temper of 4340 steel. The dashed lines show the MTS predictions. Shear tests at (a) 0.0001 s^{-1} and (b) 1000 s^{-1}.

5.1. Yield stress versus plastic strain

Fig. 14(a) shows the yield stress versus plastic strain curves predicted by the MTS and JC models for various strain rates. The initial temperature is 600 K and adiabatic heating is assumed for strain rates above 500 s^{-1}. The strain rate dependence of the yield stress is less pronounced for the MTS model than for the JC model. The hardening rate is higher at low strain rates for the JC model. The rapid increase in the yield stress that is expected at strain rates above 1000 s^{-1} (Nicholas, 1981) is not predicted by either model. This is probably due to the limited high rate data used to determine the MTS model parameters.

The temperature dependence of the yield stress for a strain rate of 1000 s^{-1} is shown in Fig. 14(b). Both models predict similar stress–strain responses as a function of temperature. However, the initial yield stress is higher and the initial hardening rate lower for the MTS model than that predicted by the JC model for initial temperatures of 300 K and 700 K. For the high temperature data, the MTS model predicts lower yield stresses.

5.2. Yield stress versus strain rate

The strain rate dependence of the yield stress (at a temperature of 600 K) predicted by the MTS and JC models is shown in Fig. 15(a). The JC model shows a higher amount of strain hardening than the MTS model. The strain rate hardening of the MTS model appears to be closer to experimental observations (Nicholas, 1981) than the JC model.

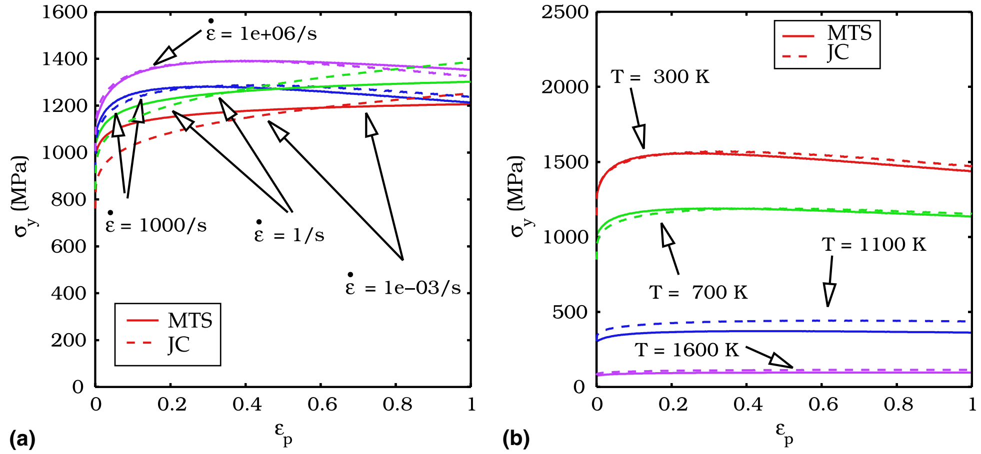

Fig. 14. Comparison of MTS and JC predictions of yield stress versus plastic strain at various strain rates and temperatures. (a) Temperature = 600 K and (b) strain rate = 1000 s^{-1}.

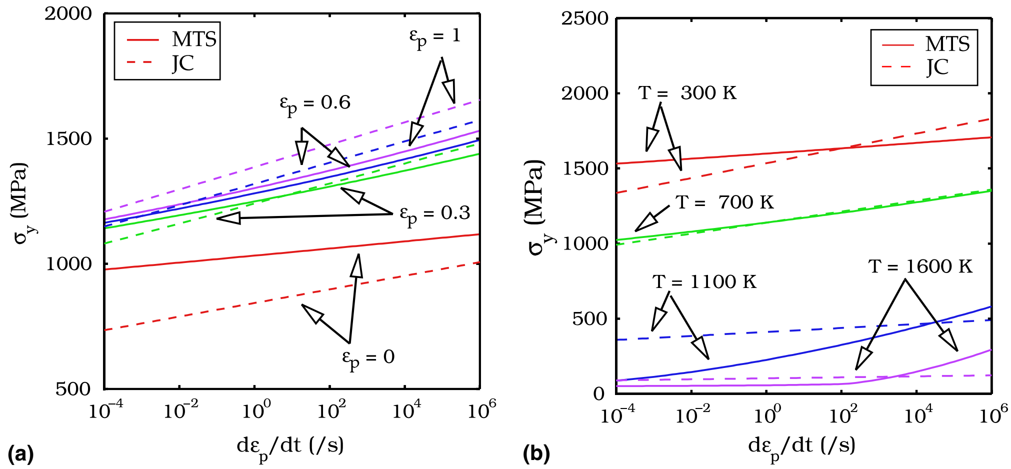

Fig. 15. Comparison of MTS and JC predictions of yield stress versus strain rate at various strain rates and temperatures. (a) Temperature = 600 K and (b) plastic strain = 0.3.

The temperature and strain rate dependence of the yield stress at a plastic strain of 0.3 is shown in Fig. 15(b). Above the phase transition temperature (1040 K), the MTS model predicts more strain rate hardening than the JC model. However, at 700 K, both models predict quite similar yield stresses. At room temperature, the JC model predicts a higher rate of strain rate hardening than the MTS model and is qualitatively closer to experimental observations.

5.3. Yield stress versus temperature

The temperature dependence of the yield stress for various plastic strains (at a strain rate of 1000 s^{-1}) is shown in Fig. 16(a). The sharp change in the value of the yield stress at the phase transition temperature may be problematic for Newton methods used in the determination of the plastic strain rate. We suggest that at temperatures close to the phase transition temperature, the high temperature parameters should be used in numerical computations. The figures show that both the models predict similar rates of temperature dependence of the yield stress.

The temperature dependence of the yield stress for various strain rates (at a plastic strain of 0.3) is shown in Fig. 16(b). In this case, the MTS model predicts at smaller strain rate effect at low temperatures than the JC

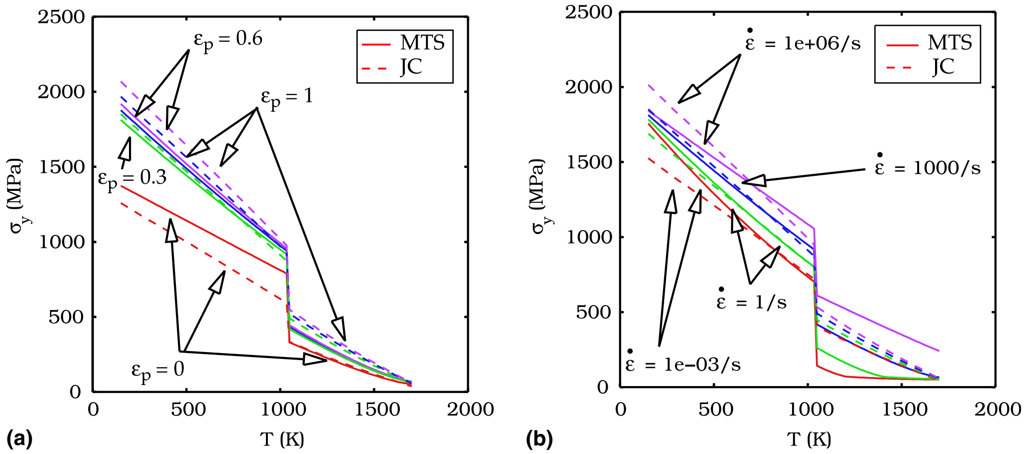

Fig. 16. Comparison of MTS and JC predictions of yield stress versus temperature at various plastic strains and strain rates. (a) Strain rate = 1000 s^{-1} and (b) plastic strain = 0.3.

model. The strain rate dependence of the yield stress increases with temperature for the MTS model while it decreases with temperature for the JC model. The JC model appears to predict a more realistic behavior because the thermal activation energy for dislocation motion is quite low at high temperatures. However, the MTS model fits high temperature/high strain rate experimental data better than the JC model and we might be observing the correct behavior in the MTS model.

5.4. Taylor impact tests

For further confirmation of the effectiveness of the MTS model, we have simulated three-dimensional Taylor impact tests using the Uintah code. Details of the code and the algorithm used can be found in Banerjee (2004). A temperature dependent specific heat model, the Nadal–Le Poac (NP) shear modulus model, the Burakovsky–Preston–Silbar (BPS) melting temperature model, and the Mie–Grüneisen equation of state have been used in these calculations (see Appendix A for more details).

It is well known that the final length of a Taylor impact cylinder scales with the initial velocity. Fig. 17 shows some experimental data on the final length of cylindrical Taylor impact specimens as a function of

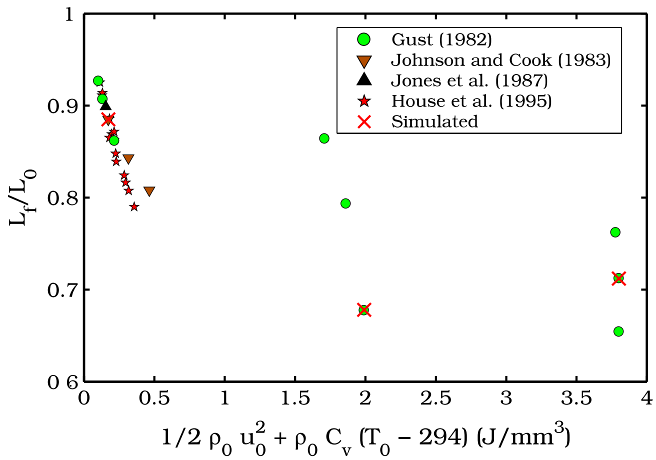

Fig. 17. The ratio of the final length to the initial length of Taylor impact specimens as a function of initial energy density. The experimental data are from Gust (1982), Johnson and Cook (1983), Jones and Gillis (1987), and House et al. (1995). The tests that we have simulated are marked with crosses.

initial velocity. We are interested in temperatures higher than room temperature. For clarity, we have separated the high temperature tests from the room temperature tests in the figure by adding an initial internal energy component to the initial kinetic energy density. We have simulated three Taylor tests at three energy levels (marked with crosses on the plot).

The four cases that we have simulated have the following initial conditions:

(1) *Case 1:* $R_c = 30$; $L_0 = 25.4$ mm; $D_0 = 7.62$ mm; $U_0 = 208$ m/s; $T_0 = 298$ K; Source: Johnson and Cook (1983).
(2) *Case 2:* $R_c = 40$; $L_0 = 30.0$ mm; $D_0 = 6.0$ mm; $U_0 = 312$ m/s; $T_0 = 725$ K; Source: Gust (1982).
(3) *Case 3:* $R_c = 40$; $L_0 = 30.0$ mm; $D_0 = 6.0$ mm; $U_0 = 160$ m/s; $T_0 = 1285$ K; Source: Gust (1982).
(4) *Case 4:* $R_c = 40$; $L_0 = 30.0$ mm; $D_0 = 6.0$ mm; $U_0 = 512$ m/s; $T_0 = 725$ K.

The MTS model parameters for the R_c 30 temper of 4340 steel have been given earlier. The MTS parameters for the R_c 40 temper of 4340 steel can be calculated either using the linear fit for various hardness levels (shown in Fig. 3) or by a linear interpolation between the R_c 38 and the R_c 45 values. MTS model parameters at temperatures above 1040 K take the high temperature values for both tempers. The initial yield stress in the Johnson–Cook model is obtained from the R_c–σ_0 relation given in Appendix B.

The computed final profiles of the Taylor impact cylinders are compared with the experimental data in Fig. 18(a)–(d).

For the room temperature test (Fig. 18(a)), the Johnson–Cook model accurately predicts the final length, the mushroom diameter, and the overall profile. The MTS model underestimates the mushroom diameter by 0.25 mm. This difference is within experimental variation (see House et al., 1995).

The simulations at 725 K (Fig. 18(b)) overestimate the final length of the specimen. The legend shows two MTS predictions for this case – MTS (1) and MTS (2). MTS (1) uses parameters σ_i and g_{0i} that have been obtained using the fits shown in Fig. 3. MTS (2) used parameters obtained by linear interpolation between the R_c 38 and R_c 45 values. The MTS (2) simulation predicts a final length that is slightly less than that predicted by the MTS (1) and Johnson–Cook models. The mushroom diameter is also slightly larger for the MTS (2) simulation.

The final length of the specimen for Case 2 is not predicted accurately by either model. We have confirmed that this error is not due to discretization (note that volumetric locking does not occur with the explicit Material Point Method used in the simulations). Plots of energy and momentum have also shown that both quantities are conserved in these simulations. The final mushroom diameter is not provided by Gust (1982). However, the author mentions that no fracture was observed in the specimen – discounting a smaller final length due to fracture. In the absence of more extensive high temperature Taylor impact data it is unclear if the error is within experimental variation or due to a fault with the models used.

The third case (Fig. 18(c)) was simulated at an initial temperature of 1285 K (above the α–γ phase transition temperature of iron). The MTS and Johnson–Cook models predict almost exactly the same behavior for this case. The final length is overestimated by both the models. Notice that the final lengths shown in Fig. 17 at or near this temperature and for similar initial velocities vary between 0.65 and 0.75 of the initial length. The simulations predict a final length that is approximately 0.77 times the initial length – which is to the higher end of the range of expected final lengths.

In all three cases, the predictions from the MTS and the Johnson–Cook models are nearly identical. To determine if any significant difference between the predictions of these models can be observed at higher strain rates, we simulated the geometry of Case 2 with a initial velocity of 512 m/s. The resulting profiles predicted by the MTS and the Johnson–Cook models are shown in Fig. 18(d). In this case, the MTS model predicts a slightly wider mushroom than the Johnson–Cook model. The final predicted lengths are almost identical. Interestingly, the amount of strain hardening predicted by the MTS model is smaller than that predicted by the Johnson–Cook model (as can be observed from the secondary bulge in the cylinder above the mushroom). We conclude that the Johnson–Cook and MTS models presented in this paper show almost identical elastic–plastic behavior in the range of conditions explored. Note that quite different sets of data were used to determine the parameters of these models and hence the similarity of the results may indicate the underlying accuracy of the parameters.

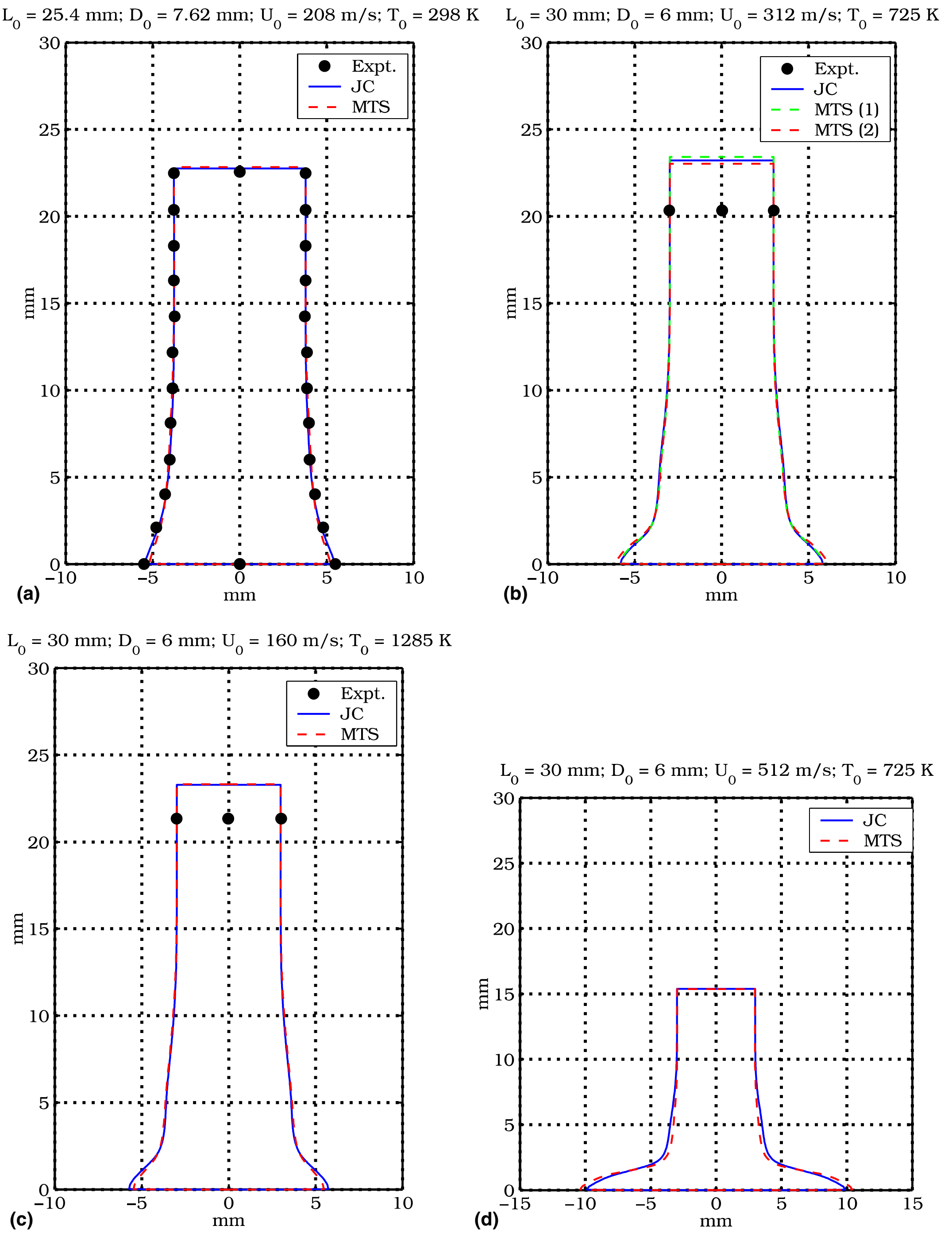

Fig. 18. Comparison of MTS and JC predictions of final Taylor specimen profiles with experimental results. (a) Case 1, (b) case 2, (c) case 3 and (d) case 4.

6. Remarks and conclusions

We have determined parameters for the Mechanical Threshold Stress model and the Johnson–Cook model for various tempers of 4340 steel. The predictions of the MTS model have been compared with experimental uniaxial stress–strain data. Yield stresses predicted by the Johnson–Cook and the MTS model have been compared for a range of strain rates and temperatures. Taylor impact tests have been simulated and the predicted profiles have been compared with experimental data.

Some conclusions regarding that follow from this work are:

(1) The MTS and Johnson–Cook models predict similar stress–strain behaviors over a large range of strain rates and temperatures. Noting that the parameters for these models have been obtained from different sets of experimental data, the similarity of the results, especially in the Taylor test simulations, is remarkable. We suggest that this is an indication of the accuracy of the models and the simulations. However, the Taylor impact tests show that both models predict lower strains at high temperatures than experiments suggest.
(2) The MTS model parameters are considerably easier to obtain than the Johnson–Cook parameters. However, the MTS simulations of the Taylor impact tests take approximately 1.5 times longer than the Johnson–Cook simulations. This is partly because the shear modulus and melting temperature models are not evaluated in the Johnson–Cook model simulations. Also, the MTS model involves more floating point operations than the Johnson–Cook model. The Johnson–Cook model is numerically more efficient than the MTS model and is preferable for large numerical simulations involving 4340 steel.
(3) The relations between the Rockwell C hardness and the model parameters that have been presented provide reasonable estimates of the parameters. However, more data for the R_c 30, 45, and 49 tempers are needed for better estimates for intermediate tempers. There is an anomaly in the strain rate and temperature dependence of the yield strength for R_c 50 and higher tempers of 4340 steel. We would suggest that the values for R_c 49 steel be used for harder tempers. For tempers below R_c 30, the fits discussed earlier provide reasonable estimates of the yield stress.
(4) The strain hardening (Voce) rule in the MTS model may be a major weakness of the model and needs to be replaced with a more physically based approach. The experimental data used to determine the strain hardening rate parameters appear to deviate significantly from Voce behavior in some cases.
(5) The determination of the values of g_{0es} and σ_{0es} involves a Fisher type modified Arrhenius plot. We have observed that the experimental data for the R_c 45 and R_c 49 tempers do not tend to reflect an Arrhenius relationship. More experimental data (and information on the variation of the experimental data) are needed to confirm this anomaly.
(6) The Nadal–Le Poac shear modulus model and the Burakovsky–Preston–Silbar melting temperature model involve less data fitting and are the suggested models for simulations over a large range of temperatures and strain rates. The specific heat model that we have presented leads to better predictions of the rate of temperature increase close to the α–γ phase transition of iron. The shear modulus and melt temperature models are also valid in the range of strain rates of the order of $10^8\ s^{-1}$.

Acknowledgements

This work was funded by the US Department of Energy through the ASCI Center for the Simulation of Accidental Fires and Explosions, under grant W-7405-ENG-48. The author gratefully acknowledges Dr. James Guilkey and Professor Patrick McMurtry for lively discussions and technical support during the course of this work.

Appendix A. Models

In this appendix, we present the parameters for some models of specific heat, melting temperature, shear modulus, and the equation of state that we have examined. We also validate these models against experimental data. The accuracy of the yield stress predicted by the MTS model depends on the accuracy of the shear modulus, melting temperature, equation of state, and specific heat models.

The models discussed in this appendix are

(1) *Specific heat*: the Lederman–Salamon–Shacklette model.
(2) *Melting temperature*: the Steinberg–Cochran–Guinan (SCG) model and the Burakovsky–Preston–Silbar (BPS) model.

(3) *Shear modulus*: the Varshni–Chen–Gray model (referred to as the MTS shear modulus model in this paper), the Steinberg–Cochran–Guinan (SCG) model, and the Nadal–Le Poac (NP) model.
(4) *Equation of state*: the Mie–Grüneisen model.

The following comparisons show why we have chosen to use a temperature dependent specific heat model, the BPS melting temperature model, the NP shear modulus model, and the Mie–Grüneisen equation of state model in our simulations.

A.1. Specific heat model for 4340 steel

A part of the plastic work done is converted into heat and used to update the temperature. The increase in temperature (ΔT) due to an increment in plastic strain ($\Delta\epsilon_p$) is given by the equation

$$\Delta T = \frac{\chi\sigma_y}{\rho C_p}\Delta\epsilon_p \tag{A.1}$$

where χ is the Taylor–Quinney coefficient, and C_p is the specific heat. The value of the Taylor–Quinney coefficient is taken to be 0.9 in all our simulations.

The relation for the dependence of C_p upon temperature that is used in this paper has the form (Lederman et al., 1974)

$$C_p = \begin{cases} A_1 + B_1 t + C_1 |t|^{-\alpha} & \text{if } T < T_c \\ A_2 + B_2 t + C_2 t^{-\alpha'} & \text{if } T > T_c \end{cases} \tag{A.2}$$

$$t = \frac{T}{T_c} - 1 \tag{A.3}$$

where T_c is the critical temperature at which the phase transformation from the α to the γ phase takes place, and A_1, A_2, B_1, B_2, α, α' are constants.

The parameters for the specific heat model (Eq. (A.2)) were fit with a least squares technique and are shown in Table A.1. A comparison of the predicted and experimental values of specific heat is shown in Fig. A.1. The transition from the bcc α phase to the fcc γ phase is clearly visible in the figure. If we use a constant (room temperature) specific heat for 4340 steel, there will be an unrealistic increase in temperature close to the phase transition which can cause premature melting in numerical simulations (and the associated numerical problems). We have chosen to use the temperature dependent specific heat model to avoid such issues.

A.2. Melting temperature model for 4340 steel

A.2.1. Steinberg–Cochran–Guinan model

The Steinberg–Cochran–Guinan (SCG) melting temperature model (Steinberg et al., 1980) is based on a modified Lindemann law and has the form

$$T_m(\rho) = T_{m0} \exp\left[2a\left(1 - \frac{1}{\eta}\right)\right]\eta^{2(\Gamma_0 - a - 1/3)}; \tag{A.4}$$

where T_{m0} is the melt temperature at $\eta = 1$, a is the coefficient of a first order volume correction to the Grüneisen gamma (Γ_0).

Table A.1
Constants used in specific heat model for 4340 steel

T_c (K)	A_1 (J/kg K)	B_1 (J/kg K)	C_1 (J/kg K)	α	A_2 (J/kg K)	B_2 (J/kg K)	C_2 (J/kg K)	α'
1040	190.14	-273.75	418.30	0.20	465.21	267.52	58.16	0.35

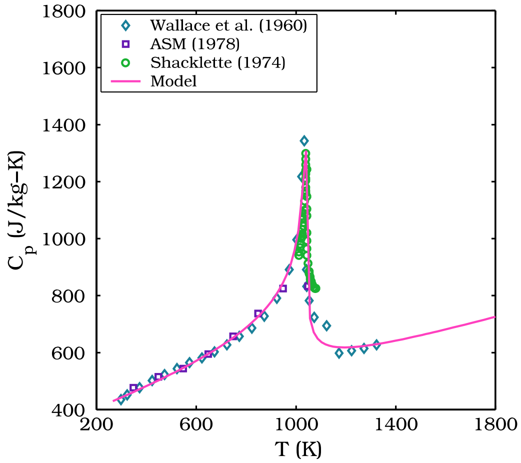

Fig. A.1. Specific heat for 4340 steel as a function of temperature. The experimental data are for iron (Wallace et al., 1960; Shacklette, 1974) and AISI 3040 steel (Steiner, 1990).

A.2.2. Burakovsky–Preston–Silbar model

The Burakovsky–Preston–Silbar (BPS) model is based on dislocation-mediated phase transitions (Burakovsky et al., 2000a). The BPS model has the form

$$T_m(p) = T_m(0)\left[\frac{1}{\zeta} + \frac{1}{\zeta^{4/3}}\frac{\mu_0'}{\mu_0}p\right]; \quad \zeta = \left(1 + \frac{K_0'}{K_0}p\right)^{1/K_0'} \tag{A.5}$$

$$T_m(0) = \frac{\kappa\lambda\mu_0 v_{WS}}{8\pi\ln(z-1)k_b}\ln\left(\frac{\alpha^2}{4b^2\rho_c(T_m)}\right); \quad \lambda = b^3/v_{WS} \tag{A.6}$$

where ζ is the compression, μ_0 is the shear modulus at room temperature and zero pressure, $\mu_0' = \partial\mu/\partial p$ is the pressure derivative of the shear modulus at zero pressure, K_0 is the bulk modulus at room temperature and zero pressure, $K_0' = \partial K/\partial p$ is the pressure derivative of the bulk modulus at zero pressure, κ is a constant, v_{WS} is the Wigner–Seitz volume, z is the crystal coordination number, α is a constant, and $\rho_c(T_m)$ is the critical density of dislocations. Note that ζ in the BPS model is derived from the Murnaghan equation of state with pressure as an input and may be different from η in numerical computations.

The parameters used for the models are shown in Table A.2. An initial density (ρ_0) of 7830 kg/m^3 has been used in the model calculations.

For the sake of simplicity, we do not consider a phase change in the melting temperature model and assume that the iron crystals remain bcc at all temperatures and pressures. We also assume that iron has the same melting temperature as 4340 steel.

Fig. A.2 shows the melting temperature of iron as a function of pressure. The melting curves predicted by the SCG model (Eq. (A.4)) and the BPS model (Eq. (A.5)) are shown as smooth curves on the figure. The BPS

Table A.2
Parameters used in melting temperature models for 4340 steel

Steinberg–Cochran–Guinan (SCG) model		
$T_{m0}(K)$	Γ_0	a
1793	1.67	1.67

Burakovsky–Preston–Silbar (BPS) model

K_0 (GPa)	K_0'	μ_0 (GPa)	μ_0'	κ	z	$b^2\rho_c(T_m)$	α	λ	v_{WS} (Å^3)	a (Å)
166	5.29	81.9	1.8	1	8	0.78	2.9	1.30	$a^3/2$	2.865

The SCG model parameters are from Gust (1982). The bulk and shear moduli and their derivatives have been obtained from Guinan and Steinberg (1974). The parameters for the BPS model at zero pressure have been obtained from Burakovsky and Preston (2000) and Burakovsky et al. (2000b), and the lattice constant (a) is from Jansen et al. (1984).

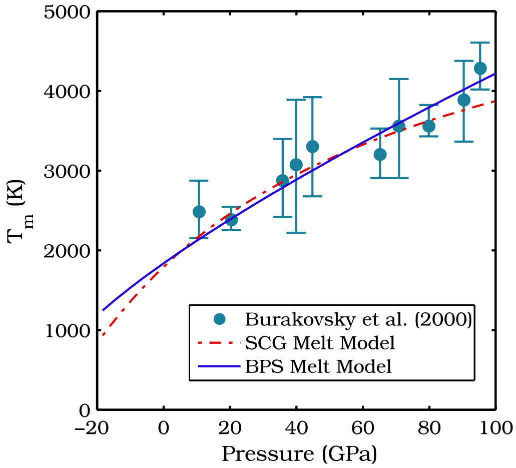

Fig. A.2. Comparison of experimental data and model predictions of the melting temperature of iron as a function of pressure. The experimental data are from Burakovsky et al. (2000a).

model performs better at high pressures, but both models are within experimental error below 100 GPa. We have chosen to use the BPS melting temperature model because of its larger range of applicability. Note that we present high pressure data because we would like these models to be applicable during the simulation of high velocity impact phenomena.

A.3. Shear modulus models for 4340 steel

A.3.1. MTS shear modulus model

The Varshni–Chen–Gray shear modulus model has been used in conjunction with the MTS plasticity models by Chen and Gray (1996) and Goto et al. (2000b). Hence, we refer to this model as the MTS shear modulus model. The MTS shear modulus model is of the form (Varshni, 1970; Chen and Gray, 1996)

$$\mu(T) = \mu_0 - \frac{D}{\exp(T_0/T) - 1} \tag{A.7}$$

where μ_0 is the shear modulus at 0 K, and D, T_0 are material constants. There is no pressure dependence of the shear modulus in the MTS shear modulus model.

A.3.2. Steinberg–Cochran–Guinan model

The Steinberg–Guinan (SCG) shear modulus model (Steinberg et al., 1980; Zocher et al., 2000) is pressure dependent and has the form

$$\mu(p,T) = \mu_0 + \frac{\partial\mu}{\partial p}\frac{p}{\eta^{1/3}} - \frac{\partial\mu}{\partial T}(T - 300); \quad \eta = \rho/\rho_0 \tag{A.8}$$

where μ_0 is the shear modulus at the reference state ($T = 300$ K, $p = 0$, $\eta = 1$). When the temperature is above T_m, the shear modulus is instantaneously set to zero in this model.

A.3.3. Nadal–Le Poac model

A modified version of the SCG model has been developed by Nadal and Le Poac (2003) that attempts to capture the sudden drop in the shear modulus close to the melting temperature in a smooth manner. The Nadal–Le Poac (NP) shear modulus model has the form

$$\mu(p,T) = \frac{1}{\mathcal{J}(\widehat{T})}\left[\left(\mu_0 + \frac{\partial\mu}{\partial p}\frac{p}{\eta^{1/3}}\right)(1 - \widehat{T}) + \frac{\rho}{Cm}k_b T\right]; \quad C := \frac{(6\pi^2)^{2/3}}{3}f^2 \tag{A.9}$$

where

$$\mathscr{J}(\widehat{T}) := 1 + \exp\left[-\frac{1 + 1/\zeta}{1 + \zeta/(1 - \widehat{T})}\right] \quad \text{for } \widehat{T} := \frac{T}{T_m} \in [0, 1 + \zeta], \tag{A.10}$$

μ_0 is the shear modulus at 0 K and ambient pressure, ζ is a material parameter, m is the atomic mass, and f is the Lindemann constant.

The parameters used in the shear modulus models are shown in Table A.3. The parameters for the MTS model have been obtained from a least squares fit to the data at a compression of 1. The values of μ_0 and $\partial\mu/\partial p$ for the SCG model are from Guinan and Steinberg (1974). The derivative with respect to temperature has been chosen so as to fit the data at a compression of 1. The NP shear model parameters μ_0 and C have also been chosen to fit the data. A value of 0.57 for C is suggested by Nadal and Le Poac (2003). However, that value leads to a higher value of μ at high temperatures than suggested by the experimental data.

Fig. A.3(a)–(c) show shear moduli predicted by the MTS shear modulus model, the SCG shear modulus model, and the NP shear modulus model, respectively. Three values of compression ($\eta = 0.9, 1.0, 1.1$) are considered for each model. The pressure-dependent melting temperature has been determined using the BPS model in each case. The initial density is taken to be 7830 kg/m^3. The model predictions are compared with experimental data for AISI 1010 steel and SAE 304 stainless steel. As the figure shows, both steels behave quite similarly as far as their shear moduli are concerned. We assume that 4340 steel also shows a similar dependence of shear modulus on temperature.

The MTS model does not incorporate any pressure dependence of the shear modulus. The pressure dependence observed in Fig. A.3(a) is due to the pressure dependence of T_m. Both the SCG and NP shear modulus models are pressure dependent and provide a good fit to the data. Though the SCG model is computationally more efficient than and as accurate as the NP model, we have chosen to the NP shear modulus model for our MTS calculations for 4340 steel because of its smooth transition to zero shear modulus at melt.

A.4. Mie–Grüneisen equation of state for 4340 steel

The hydrostatic pressure (p) is calculated using a temperature-corrected Mie–Grüneisen equation of state of the form (Zocher et al., 2000), (see also Wilkins, 1999, p. 61)

$$p = \frac{\rho_0 C_0^2(\eta - 1)\left[\eta - \frac{\Gamma_0}{2}(\eta - 1)\right]}{\left[\eta - S_\alpha(\eta - 1)\right]^2} + \Gamma_0 E \tag{A.11}$$

where C_0 is the bulk speed of sound, Γ_0 is the Grüneisen's gamma at the reference state, $S_\alpha = \mathrm{d}U_s/\mathrm{d}U_p$ is a linear Hugoniot slope coefficient, U_s is the shock wave velocity, U_p is the particle velocity, and E is the internal energy per unit reference specific volume. The internal energy is computed using

$$E = \frac{1}{V_0}\int C_v \, \mathrm{d}T \approx \frac{C_v(T - T_0)}{V_0} \tag{A.12}$$

where $V_0 = 1/\rho_0$ is the reference specific volume at the reference temperature T_0.

The pressure in the steel is calculated using the Mie–Grüneisen equation of state. The Grüneisen gamma (Γ_0) is assumed to be a constant over the regime of interest. The specific heat at constant volume is assumed to be the same as that at constant pressure and is calculated using Eq. (A.2).

In the model calculations, the bulk speed of sound (C_0) is 3935 m/s and the linear Hugoniot slope coefficient (S_α) is 1.578. Both parameters are for iron and have been obtained from Brown et al. (2000). The Grüneisen

Table A.3
Parameters used in shear modulus models for 4340 steel

MTS shear modulus model			SCG shear modulus model			NP shear modulus model				
μ_0 (GPa)	D (GPa)	T_0 (K)	μ_0 (GPa)	$\partial\mu/\partial p$	$\partial\mu/\partial T$ (GPa/K)	μ_0 (GPa)	$\partial\mu/\partial p$	ζ	C	m (amu)
85.0	10.0	298	81.9	1.8	0.0387	90.0	1.8	0.04	0.080	55.947

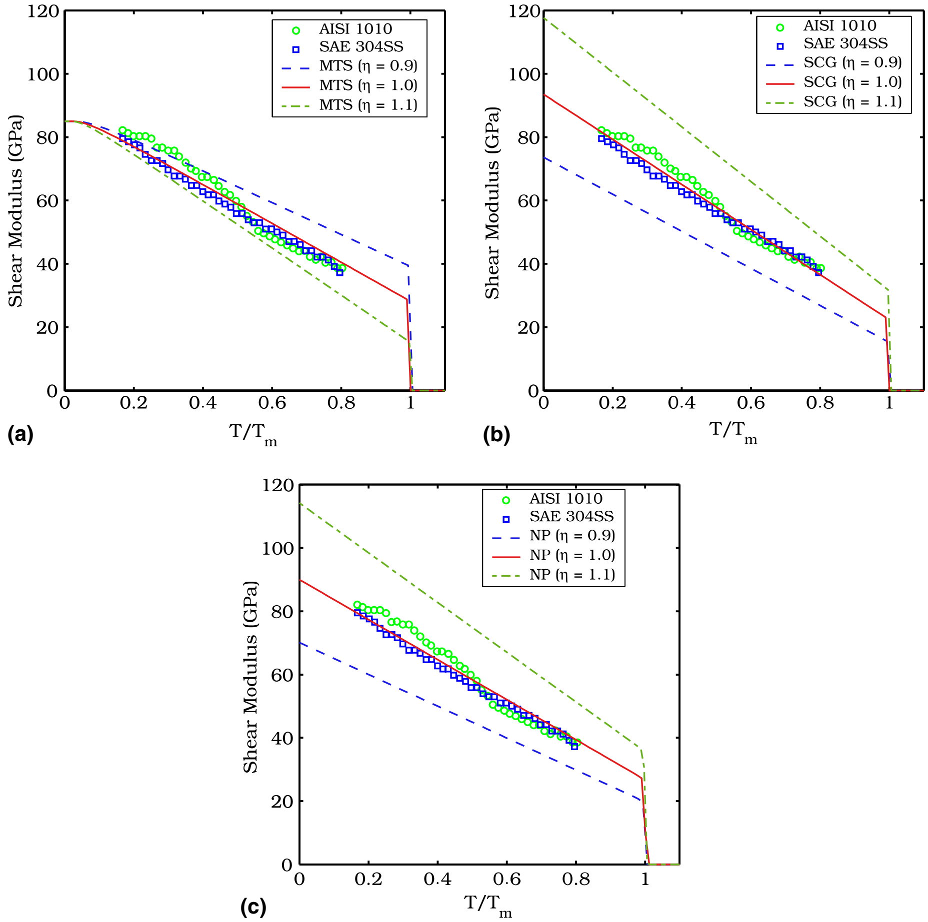

Fig. A.3. Comparison of experimental data with model predictions of shear modulus for 4340 steel. The experimental data are for AISI 1010 steel and SAE 304 stainless steel (Fukuhara and Sanpei, 1993) at standard pressure. The pressure at $\eta = 1.1$ is approximately 15 GPa at room temperature and 30 GPa at the melting temperature. The hydrostatic pressure at $\eta = 0.9$ is approximately −10 GPa at room temperature and around 5 GPa at melt. (a) MTS shear model, (b) SCG shear model and (c) NP shear model.

gamma value ($\Gamma_0 = 1.69$) has been interpolated from values given by Gust et al. (1979). An initial temperature (T_0) of 300 K and an initial density of 7830 kg/m^3 have been used in the model calculations.

Appendix B. Johnson–Cook model and parameters

The Johnson–Cook (JC) model (Johnson and Cook, 1983) is purely empirical and has the form

$$\sigma_y(\epsilon_p, \dot{\epsilon}, T) = \sigma_0\left[1 + \frac{B}{\sigma_0}(\epsilon_p)^n\right][1 + C\ln(\dot{\epsilon}^*)][1 - (T^*)^m] \tag{B.1}$$

$$\dot{\epsilon}^* = \frac{\dot{\epsilon}}{\dot{\epsilon}_0}; \quad T^* = \frac{(T - T_r)}{(T_m - T_r)} \tag{B.2}$$

where σ_0 is the yield stress at zero plastic strain, and (B,C,n,m) are material constants, $\dot{\epsilon}_0$ is a reference strain rate, and T_r is a reference temperature.

The value of σ_0 for 4340 steel in the Johnson–Cook model varies with the temper of the steel. We have fit the yield stress versus R_c hardness curve for 4340 steel from the ASM Handbook (Steiner, 1990) to determine the value of σ_0 for various tempers. The equation for the fit is

$$\sigma_0 = \exp(A_1 R_c + A_2)(\text{MPa}) \tag{B.3}$$

where $A_1 = 0.0355$ ln(MPa), $A_2 = 5.5312$ ln(MPa), and R_c is the Rockwell C hardness of the steel. The value of $B/\sigma_0 = 0.6339$ is assumed to be a constant for all tempers. The strain hardening exponent (n) is 0.26 and the strain rate dependence parameter (C) is 0.014, for all tempers. The reference strain rate $\dot{\epsilon}_0$ is 1 s^{-1}. For temperatures less than 298 K, thermal softening is assumed to be linear and the parameter m takes a value of 1. Above 298 K and lower than 1040 K, m is assumed to be 1.03, and beyond 1040 K, m is taken as 0.5 (Lee and Yeh, 1997). The reference temperature (T_r) is 298 K and the melt temperature (T_m) is kept fixed at 1793 K. These parameters provide a reasonable fit to the experimental data presented earlier in the context of the MTS model.

References

Banerjee, B., 2004. Material point method simulations of fragmenting cylinders. In: Proc. 17th ASCE Engineering Mechanics Conference (EM2004), Newark, Delaware.

Banerjee, B., 2005. The Mechanical threshold stress model for various tempers of 4340 steel, arXiv:cond-mat 0510330, pp. 1–39.

Brown, W.F., Mindlin, H., Ho, C.Y., 1996. Aerospace Structural Metals Handbook, vol. 1: Code 1206. CINDAS/USAF CRDA Handbooks Operation, Purdue University, West Lafayette, IN.

Brown, J.M., Fritz, J.N., Hixson, R.S., 2000. Hugoniot data for iron. J. Appl. Phys. 88 (9), 5496–5498.

Burakovsky, L., Preston, D.L., 2000. Analysis of dislocation mechanism for melting of elements. Solid State Commun. 115, 341–345.

Burakovsky, L., Preston, D.L., Silbar, R.R., 2000a. Analysis of dislocation mechanism for melting of elements: pressure dependence. J. Appl. Phys. 88 (11), 6294–6301.

Burakovsky, L., Preston, D.L., Silbar, R.R., 2000b. Melting as a dislocation-mediated phase transition. Phys. Rev. B 61 (22), 15011–15018.

Caillard, D., Martin, J.L., 2003. Thermally Activated Mechanisms in Crystal Plasticity. Pergamon, Amsterdam.

Chen, S.R., Gray, G.T., 1996. Constitutive behavior of tantalum and tantalum–tungsten alloys. Metall. Mater. Trans. A 27, 2994–3006.

Chi, Y.C., Lee, S., Cho, K., Duffy, J., 1989. The effect of tempering and test temperature on the dynamic fracture initiation behavior of an AISI 4340 VAR steel. Mater. Sci. Eng. A 114, 105–126.

Cottrell, A.H., Bilby, B.A., 1949. Dislocation theory of yielding and strain aging of iron. Proc. Phys. Soc. London A 62, 49–62.

Follansbee, P.S., Kocks, U.F., 1988. A constitutive description of the deformation of copper based on the use of the mechanical threshold stress as an internal state variable. Acta Metall. 36, 82–93.

Fukuhara, M., Sanpei, A., 1993. Elastic moduli and internal friction of low carbon and stainless steels as a function of temperature. ISIJ Int. 33 (4), 508–512.

Goto, D.M., Bingert, J.F., Chen, S.R., Gray, G.T., Garrett, R.K., 2000a. The mechanical threshold stress constitutive-strength model description of HY-100 steel. Metall. Mater. Trans. A 31, 1985–1996.

Goto, D.M., Bingert, J.F., Reed, W.R., Garrett, R.K., 2000b. Anisotropy-corrected MTS constitutive strength modeling in HY-100 steel. Scr. Mater. 42, 1125–1131.

Guinan, M.W., Steinberg, D.J., 1974. Pressure and temperature derivatives of the isotropic polycrystalline shear modulus for 65 elements. J. Phys. Chem. Solids 35, 1501–1512.

Gust, W.H., 1982. High impact deformation of metal cylinders at elevated temperatures. J. Appl. Phys. 53 (5), 3566–3575.

Gust, W.H., Steinberg, D.J., Young, D.A., 1979. Hugoniot parameters to 320 GPa for three types of steel. High Temp. High Pressure 11, 271–280.

Hanson, K.M., 2005. Inference about the plastic behavior of materials from experimental data. In: Hanson, K.M., Hemez, F.M. (Eds.), Sensitivity Analysis of Model Output. Los Alamos Research Library, Los Alamos, NM, pp. 126–136.

House, J.W., Lewis, J.C., Gillis, P.P., Wilson, L.L., 1995. Estimation of the flow stress under high rate plastic deformation. Int. J. Impact Eng. 16 (2), 189–200.

Jansen, H.J.F., Hathaway, K.B., Freeman, A.J., 1984. Structural properties of ferromagnetic bcc iron: a failure of the local-spin-density approximation. Phys. Rev. B 30 (10), 6177–6179, lattice constant for bcc iron.

Johnson, G.R., Cook, W.H., 1983. A constitutive model and data for metals subjected to large strains, high strain rates and high temperatures. In: Proc. 7th International Symposium on Ballistics, pp. 541–547.

Johnson, G.R., Cook, W.H., 1985. Fracture characteristics of three metals subjected to various strains, strain rates, temperatures and pressures. Int. J. Eng. Fract. Mech. 21, 31–48.

Jones, S.E., Gillis, P.P., 1987. On the equation of motion of the undeformed section of a Taylor impact specimen. J. Appl. Phys. 61 (2), 499–502.

Kocks, U.F., 2001. Realistic constitutive relations for metal plasticity. Mater. Sci. Eng. A 317, 181–187.

Kocks, U.F., Argon, A.S., Ashby, M.F., 1975. Thermodynamics and Kinetics of Slip. Pergamon Press, Oxford.

Larson, F.R., Nunes, J., 1961. Low temperature flow and fracture tension properties of heat treated SAE 4340 steel. Trans. ASM 53, 663–682.

Lederman, F.L., Salamon, M.B., Shacklette, L.W., 1974. Experimental verification of scaling and test of the universality hypothesis from specific heat data. Phys. Rev. B 9 (7), 2981–2988.

Lee, W.-S., Yeh, G.-W., 1997. The plastic deformation behavior of AISI 4340 alloy steel subjected to high temperature and high strain rate loading conditions. J. Mater. Proc. Tech. 71, 224–234.

Nadal, M.-H., Le Poac, P., 2003. Continuous model for the shear modulus as a function of pressure and temperature up to the melting point: analysis and ultrasonic validation. J. Appl. Phys. 93 (5), 2472–2480.

Nemat-Nasser, S., 2004. Plasticity: A Treatise on Finite Deformation of Heterogeneous Inelastic Materials. Cambridge University Press, Cambridge.

Nicholas, T., 1981. Tensile testing of materials at high rates of strain. Exp. Mech. 21, 117–185.

Shacklette, L.W., 1974. Specific heat and resistivity of iron near its Curie point. Phys. Rev. B 9 (9), 3789–3792.

Steinberg, D.J., Cochran, S.G., Guinan, M.W., 1980. A constitutive model for metals applicable at high-strain rate. J. Appl. Phys. 51 (3), 1498–1504.

Steiner, R., 1990. American Society of Metals Handbook, vol. 1. American Society of Metals, New York.

Tanimura, S., Duffy, J., 1986. Strain rate effects and temperature history effects for three different tempers of 4340 VAR steel. Int. J. Plast. 2, 21–35.

Varshni, Y.P., 1970. Temperature dependence of the elastic constants. Phys. Rev. B 2 (10), 3952–3958.

Wallace, D.C., Sidles, P.H., Danielson, G.C., 1960. Specific heat of high purity iron by a pulse heating method. J. Appl. Phys. 31 (1), 168–176.

Wilkins, M.L., 1999. Computer Simulation of Dynamic Phenomena. Springer-Verlag, Berlin.

Zerilli, F.J., Armstrong, R.W., 1987. Dislocation-mechanics-based constitutive relations for material dynamics calculations. J. Appl. Phys. 61 (5), 1816–1825.

Zocher, M.A., Maudlin, P.J., Chen, S.R., Flower-Maudlin, E.C., 2000. An evaluation of several hardening models using Taylor cylinder impact data. In: Proc., European Congress on Computational Methods in Applied Sciences and Engineering, ECCOMAS, Barcelona, Spain.